How to cite: *Angew. Chem. Int. Ed.* **2026**, e18906
doi.org/10.1002/anie.202518906

Batteries

Unlocking Full State-of-Charge of Polyoxometalate for High-Energy-Density Redox Flow Batteries via Concerted Proton-Electron Transfer

Mingjun Han, Yuyang Liu, Wenjihao Hu, Wei Sun, Jun Yan, Qiusheng Zhou, Jian Luo, Lei Gan, Jianye Liu, Chenyang Zhang, Jie Li,* and Xiaobin Li*

Abstract: Polyoxometalates (POMs) exhibit exceptional multi-electron transfer capacity for next-generation high-energy-density redox flow batteries (RFBs), while their operable state-of-charge (SoC, ≤33.3%) is commonly limited by universal highly reduced metastable states under proton-starved conditions. Herein, by establishing a proton-coupled electron transfer (PCET) paradigm for $[P_2W_{18}O_{62}]^{6-}$ ($\{P_2W_{18}\}$) cluster, we reveal that protonation at oxygen sites stabilizes reduced tungsten sites via concerted proton-electron transfer (CPET). Marcus theory combined with DFT calculations quantifies the thermodynamic driving force and kinetic barrier for region-selective CPET processes, and operando analyses by pH monitoring and Raman spectroscopy further confirm this proton-coupled reversible redox mechanism. Guided by these findings, we engineer the high-proton-activity $H_6\{P_2W_{18}\}$ negolyte paired with a $VOSO_4$-based posolyte and stepwise charging-discharging protocol that enables stable full SoC operation. The resulting RFBs achieve unprecedented performance, which maintains 95.04 Ah L^{-1} without decay over 600 cycles (over 1020 h) at 66.7% SoC of 0.3 M $H_6\{P_2W_{18}\}$, and 141.75 Ah L^{-1} at 100% SoC of 0.3 M $H_6\{P_2W_{18}\}$, as well as delivers a record-breaking 236.03 Ah L^{-1} and 239.02 Wh L^{-1} at 100% SoC of 0.5 M $H_6\{P_2W_{18}\}$. This work unlocks full SoC of $\{P_2W_{18}\}$ by translating CPET mechanistic insights into actionable electrolyte design, establishing a generalizable pathway toward high-energy-density POM-RFBs.

Introduction

The accelerating global transition to renewable energy, projected to supply nearly 90% electricity by 2050, has emerged as a cornerstone for combating climate change while meeting escalating energy demands.[1–3] Nevertheless, the intermittent and fluctuating nature of solar/wind generation necessitates breakthrough innovations in energy storage technologies to ensure grid reliability and maximize renewable utilization.[4] Among diverse energy storage technologies, redox flow batteries (RFBs) have emerged as one of the most promising solutions for large-scale applications due to their inherent safety, scalability enabled by decoupled power/capacity configuration, extended cycle life, and millisecond-level response characteristics.[5,6]

While commercially deployed redox flow batteries of vanadium (VRFBs), iron-chromium (Fe-Cr RFBs), and zinc-bromine (Zn-Br RFBs) continue to mature,[5,7] the scientific community is actively pioneering molecular-level engineering of next-generation redox-active electrolytes. The conventional single-/dual-electron (n = 1∼2) redox couples dominate more than 95% of existing systems, mainly including transition metal,[8–14] halogen,[15–17] polysulfides,[18–20] and organic compounds.[21–23] However, the low energy density (15∼50 Wh/L) imposed by single-/dual-electron transfer reactions restricts their potential for further development. Therefore, the exploration for stable and reversible multi-electron (n ≥ 3) transfer redox-active couples has emerged as a pivotal research frontier in RFBs innovation.

Polyoxometalates (POMs), notably Keggin-type ($[XM_{12}O_{40}]^{n-}$) and Dawson-type ($[X_2M_{18}O_{62}]^{m-}$) clusters, have become frontrunners in multi-electron redox chemistry, leveraging their unique cluster-level electron delocalization to present more than $12e^-$ transfer capacity by M^{VI}/M^{V} redox processes.[24–26] Nevertheless, studies have shown that practical electrolyte utilization (here, we indicate it by state-of-charge (SoC)) of POMs remains capped at less than 33.3%. The bottleneck of low SoC is widely present across various POM negolytes. In 2013, Anderson et al.[27] first introduced an atom-substituted $[SiV_3W_9O_{40}]^{7-}$ ($\{SiV_3W_9\}$) for symmetric RFB electrolyte, achieving 33.3% SoC of $\{SiV_3W_9\}$ negolyte ($3e^-$ transfer relative to $9e^-$ theoretical). Subsequently, Liu

[*] Dr. M. Han, Prof. J. Yan, J. Luo, Dr. L. Gan, Dr. J. Liu, Prof. J. Li
School of Chemistry and Chemical Engineering, Central South University, Changsha, Hunan 410083, China
E-mail: lijieliu@csu.edu.cn

Dr. Y. Liu
School of Public Administration, Central South University, Changsha 410083, China

Prof. W. Hu, Prof. W. Sun, Prof. C. Zhang
National Key Laboratory of Mineral Processing Science and Technology, School of Minerals Processing and Bioengineering, Central South University, Changsha, Hunan 410083, China
E-mail: zhangchenyang@csu.edu.cn

Prof. Q. Zhou, Prof. X. Li
School of Metallurgy and Environment, Central South University, Changsha 410083, China

Additional supporting information can be found online in the Supporting Information section

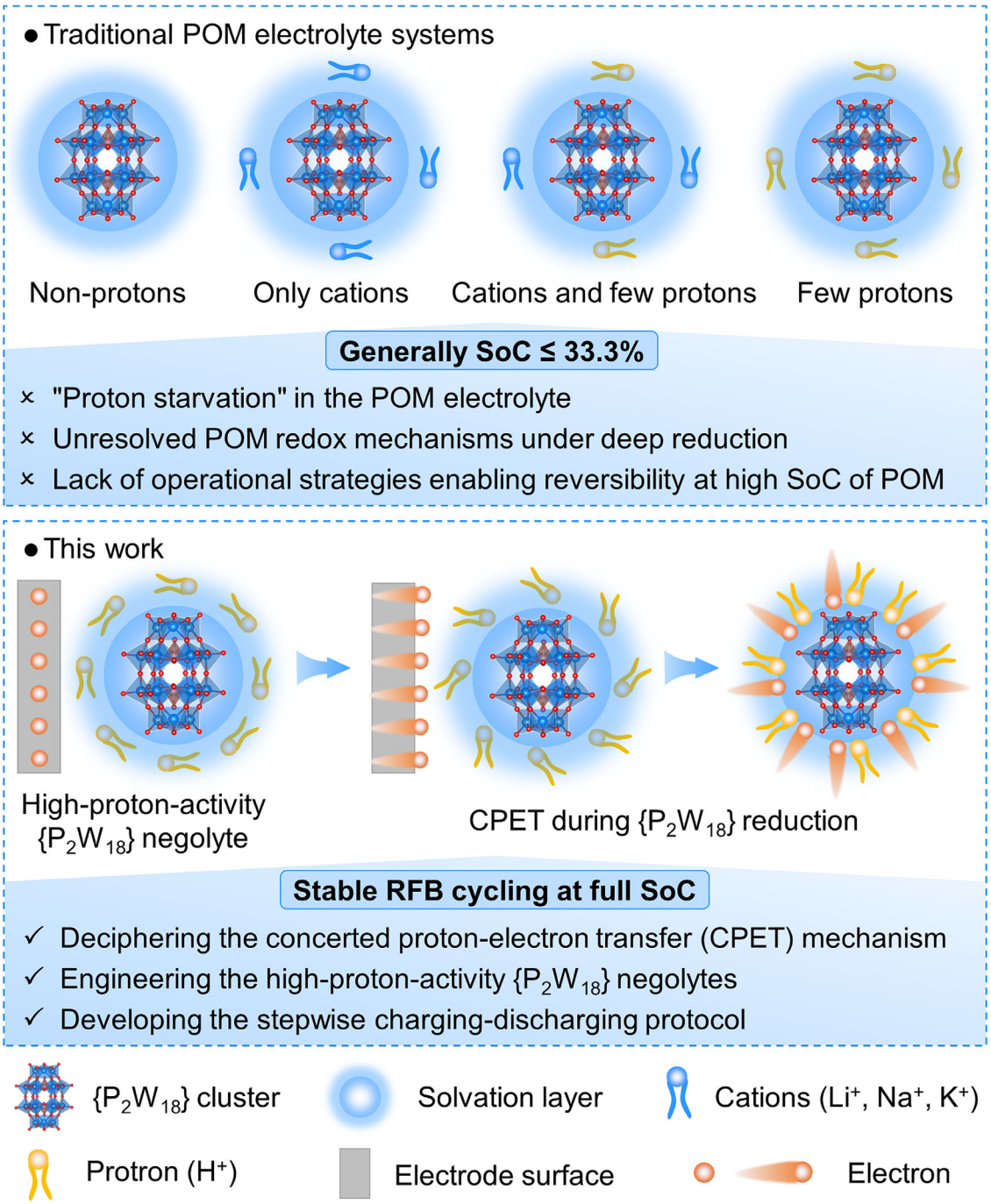

Scheme 1. The essential comparison between traditional POM electrolyte systems and this work.

et al.[28] (2016) pioneered the $H_6[CoW_{12}O_{40}]$ ($\{CoW_{12}\}$) cluster to devise the symmetric RFB with 33.3% SoC of $\{CoW_{12}\}$ negolyte ($4e^-$ transfer relative to $12e^-$ theoretical). Chen et al.[29] (2018) first employed the $Li_6[P_2W_{18}O_{62}]$ ($Li_6\{P_2W_{18}\}$) negolyte in $\{P_2W_{18}\}$||Br RFB, establishing the proof-of-concept for energy storage using highly reduced $\{P_2W_{18}\}$ cluster. However, the RFB cycling was limited to 20 cycles at ~88.9% SoC of $Li_6\{P_2W_{18}\}$ negolyte (converting the discharge capacity and Coulombic efficiency relative to $18e^-$ theoretical capacity) and the underlying redox chemistry remained insufficiently resolved. Recently, Ai et al.[30] (2022) reported the advancement of high-power-density RFB at low temperatures (−20 °C) using $H_6[P_2W_{18}O_{62}]$ ($H_6\{P_2W_{18}\}$) cluster as the negolyte at 33.3% SoC ($6e^-$ transfer relative to $18e^-$ theoretical), highlighting the robustness and practicality in a wide temperature range. In addition, it also evidenced by $[PW_{12}O_{40}]^{3-}$ ($\{PW_{12}\}$, 33.3% and 41.7% SoC, $4e^-$ and $5e^-$ transfer relative to $12e^-$ theoretical, respectively),[31,32] $[PV_{14}O_{42}]^{9-}$ ($\{PV_{14}\}$, 28.5% SoC, $4e^-$ transfer relative to $14e^-$ theoretical),[33] $[SiW_{12}O_{40}]^{4-}$ and $[BW_{12}O_{40}]^{5-}$ ($\{SiW_{12}\}$ and $\{BW_{12}\}$, 16.7% SoC, $2e^-$ transfer relative to $12e^-$ theoretical).[33,34] Therefore, it is imperative to unlock the

full SoC of POMs to break through the universal bottleneck that will represent a critical milestone toward achieving high-energy-density RFBs.

Herein, we identify that the low utilization efficiency of traditional POM electrolyte systems primarily stems from unresolved POM redox mechanisms under deep reduction and the lack of operational electrolyte strategies that enable reversibility at high SoC.[35–37] Crucially, the "proton starvation" during POM reduction processes restricts the dynamic coupling of charge storage and protonation, resulting in the accessible SoC usually less than 33.3% (Scheme 1). These critical barriers fundamentally limit the intrinsic multi-electron capacity of POMs, resulting in practical electrolyte utilizations far below their theoretical potentials. To overcome these limitations, this study established a proton-coupled electron transfer (PCET) paradigm to decipher the structure-activity relationship of $\{P_2W_{18}\}$ redox chemistry. We revealed that protonation at O sites stabilizes reduced W sites via region-selective concerted proton-electron transfer (CPET) processes. This in-depth mechanistic insight enabled the engineering of high-proton-activity $\{P_2W_{18}\}$ negolytes and developing a stepwise charging-discharging protocol (Scheme 1). The resulting RFBs further delivered unprecedented stable cycling performances at high SoC (66.7% and 100%) of $H_6\{P_2W_{18}\}$ negolyte, providing an approach to unlock full SoC for realizing reversible, durable, and high-energy-density POM-RFBs.

Results and Discussion

Electrochemical and Structural Properties of $\{P_2W_{18}\}$

Cyclic voltammetry (CV) analysis of $\{P_2W_{18}\}$ revealed four highly reversible redox couples through segmented potential window scanning, as depicted in Figure 1a, where the oxidation peaks (O_1, O_2, O_3, O_4) and reduction peaks (R_1, R_2, R_3, R_4) are labeled sequentially. The characteristic peaks of O_1/R_1 to O_4/R_4 redox couples were observed at 0.293 V/0.228 V, 0.148 V/0.090 V, − 0.115 V/− 0.166 V, − 0.350 V/− 0.397 V versus SHE, respectively. These redox events originate from approximately six-electron transfers (sequence of 1, 1, 2, 2) within the $\{W_{18}O_{54}\}$ shell of $\{P_2W_{18}\}$ cluster, specifically corresponding to the redox of W^{VI}/W^{V}.[30,38] The peak separations (ΔE_p) and near-unity peak current ratios (I_{pa}/I_{pc}) confirm exceptional electrochemical reversibility across all four redox stages. It is important to note that the redox potential of $\{P_2W_{18}\}$ shows a pH-dependent directional shift in various conductive media (Figure 1b). Taking pH = 3 (Na^+-dominated systems) as reference: (1) the R_1 and R_2 reduction peaks show mild negative shifts ($\Delta E = 10 \sim 39$ mV) in H^+/Na^+-dominated systems (pH = − 0.1, 1, 2), as well as pronounced negative shifts (ΔE = 69∼102 mV) in H^+-deficient/Na^+-free systems (pH = 0.23, 1.41), demonstrating H^+ concentration modulation of O_1/R_1 and O_2/R_2 redox couples; (2) the R_3 and R_4 peaks exhibit significant positive

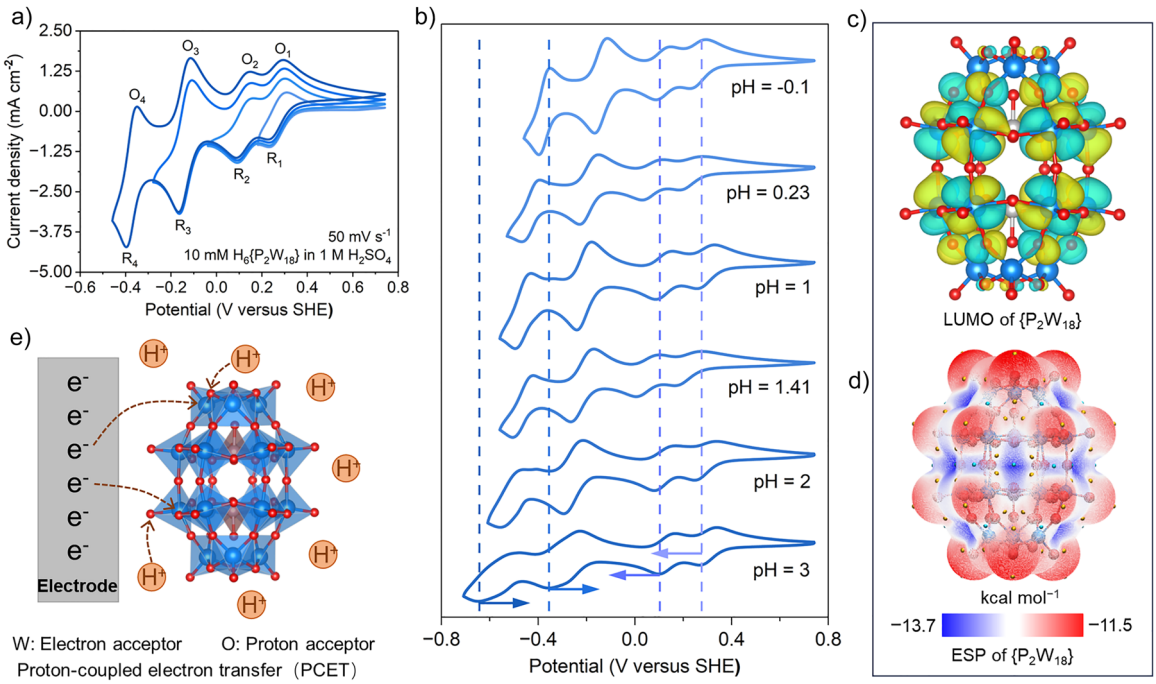

Figure 1. a) Segmented cyclic voltammetry (CV) curves of 10 mM $H_6\{P_2W_{18}\}$ in 1 M H_2SO_4 at 50 mV s^{-1}. b) CV curves of 10 mM $H_6\{P_2W_{18}\}$ in different pH media. pH = − 0.1, 10 mM $H_6\{P_2W_{18}\}$ in 1 M H_2SO_4; pH = 0.23, 10 mM $H_6\{P_2W_{18}\}$ in 0.5 M H_2SO_4; pH = 1, 10 mM $H_6\{P_2W_{18}\}$ in 0.75 M Na_2SO_4 and ∼0.25 M H_2SO_4; pH = 1.41, 10 mM $H_6\{P_2W_{18}\}$; pH = 2, 10 mM $H_6\{P_2W_{18}\}$ in 0.9 M Na_2SO_4 and adjust the pH with dilute H_2SO_4; pH = 3, 10 mM $H_6\{P_2W_{18}\}$ in 0.9 M Na_2SO_4 and adjust the pH with dilute NaOH. c) Lowest unoccupied molecular orbital (LUMO) of $\{P_2W_{18}\}$. d) Electrostatic potential (ESP) diagram of $\{P_2W_{18}\}$, the yellow and blue spheres on the surface correspond to the maximum and minimum points of the electrostatic potential, respectively. e) Schematic diagram of proton-coupled electron transfer of $\{P_2W_{18}\}$ cluster on the electrode.

shifts (ΔE = 63~251 mV) with decreasing pH (increasing H^+), indicating strong H^+ sensitivity of O_3/R_3 and O_4/R_4 redox couples. Collectively, the redox process of $\{P_2W_{18}\}$ cluster is significantly governed by H^+ (protons) content, it is speculated that the H^+-dependent behavior stems from the demand for countercharged ions and protonation during the redox processes. The redox kinetics of $H_6\{P_2W_{18}\}$ were further investigated by CV and rotating disk electrode (RDE) (Figures S4 and S5 and Table S2). These results revealed a high diffusion coefficient (D) of 2.49×10^{-6} cm^2 s^{-1} and a rapid electron transfer rate constant (k_0) of 8.9×10^{-4} cm s^{-1} (faster than that of V^{3+}/V^{2+}, 3.9×10^{-5} cm s^{-1}),[39] indicating favorable redox kinetics for electrochemical processes.

The active sites of $\{P_2W_{18}\}$ cluster could be decoupled into W-centered "electron active sites" and O-based "protonation active sites". As revealed by frontier molecular orbital analysis (Figure 1c), the spatial distribution of the lowest unoccupied molecular orbital (LUMO) in $\{P_2W_{18}\}$ predominantly localizes at W centers, attributing to their electron-deficient nature of abundant W 5d vacant orbitals. Furthermore, these electron-deficient W sites enable reversible electron storage/release through d-orbital adaptive electron filling: W^{VI} ($5d^0$) + e^- ⇌ W^V ($5d^1$). Moreover, the electrostatic potential (ESP) analysis reveals that the nucleophilic regions of $\{P_2W_{18}\}$ cluster (charge: −6) are critical for its protonation reaction. As depicted in Figure 1d, the calculated ESP isosurface exhibits a quantitative color scale range of −13.7 to −11.5 kcal/mol, with three characteristic domains.[40] The minimum ESP values (blue color) are concentrated in the middle region of the adjacent trimetallic oxygen clusters (W_3O_{15}) in $\{P_2W_{18}\}$, corresponding to the highest electron density. On the contrary, the relative maximum ESP values (red color) are distributed at the terminal oxygen (O_t in W═O_t), while the bridging oxygen (O_b in W─O_b─W) regions (white color) are between the two, reflecting a slight decrease in electron density at O_t than O_b. The narrow ESP differential between O_t and O_b indicates comparable proton affinity, thus both O_b and O_t sites of $\{P_2W_{18}\}$ cluster could serve as hydrogen-bond acceptors for protonation reactions. Therefore, Figure 1e further illustrates a possible proton-coupled electron transfer (PCET) process of $\{P_2W_{18}\}$ reduction at the electrode interface, where synergistic interactions between W-centered "electron active sites" and O_t/O_b-centered "protonation active sites" may contribute to efficient multi-electron transfer reactions.

Proton-Coupled Electron Transfer (PCET) in $\{P_2W_{18}\}$ Redox Processes

The complicated $18e^-$ transfer scheme of $\{P_2W_{18}\}$ operates through proton-coupled electron transfer (PCET) processes, the reaction network diagram as plotted in Figure 2a, with three dominant pathways of CPET, sequential proton-electron transfer (SPET), and sequential electron-proton transfer (SEPT).[35] Highly reduced species without protonation and excessively protonated species without reduction are restricted by electrostatic repulsion and proton saturation, respectively, which can cause irreversible deformation or even collapse of cluster structures. Therefore, we focus on the CPET (abbreviated as C), ET (abbreviated as E) pathways, and PT (abbreviated as P) pathways during the $\{P_2W_{18}\}$ reduction and protonation processes.

Building upon the identified protonation hotspots in bridging oxygen and terminal oxygen in "cap region" and "belt region" of $\{P_2W_{18}\}$ cluster (Figure 2b, Figures S1d, S6–S9),[41] we computationally modeled the ET configurations of $\{P_2W_{18}\}$_ne and CPET configurations of $\{P_2W_{18}\}$_ne_nH ($n \leq 6$) at low reduction states, as well as the CPET configurations of $\{P_2W_{18}\}$_ne_nH ($6 < n \leq 18$) at high reduction states. As depicted in Figure 2c and Figure S10, there are 8 probable protonation pathways in CPET processes by considering the protonation of O_t and O_b in the "Cap region" and "Belt region" of $\{P_2W_{18}\}$ at high reduction states, which is corresponding to $\{P_2W_{18}\}$_ne_nH_{CBt}, $\{P_2W_{18}\}$_ne_nH_{BCt}, $\{P_2W_{18}\}$_ne_nH_{CBb}, $\{P_2W_{18}\}$_ne_nH_{BCb}, $\{P_2W_{18}\}$_ne_nH_{CbBt}, $\{P_2W_{18}\}$_ne_nH_{BtCb}, $\{P_2W_{18}\}$_ne_nH_{BbCt}, and $\{P_2W_{18}\}$_ne_nH_{CtBb}. Nevertheless, $\{P_2W_{18}\}$_ne_nH_{BbCt} and $\{P_2W_{18}\}$_ne_nH_{CtBb} pathways are excluded through thermodynamic statistical analysis in Figure S14. Gibbs free energy analysis identifies $\{P_2W_{18}\}$_ne_nH_{Bt} and $\{P_2W_{18}\}$_ne_nH_{Cb} as thermodynamically favored CPET pathways (Figures S11 and S12), thus activation energy ($\Delta G^{\neq}$) network diagram of $\{P_2W_{18}\}$_ne_nH_{CBb} and $\{P_2W_{18}\}$_ne_nH_{BCt} pathways via CPET process have been systematically investigated by Marcus theory and density functional theory (DFT) calculations in Figure S15. These results indicate the two-stage evolution of the $\Delta G^{\neq}$ in the CPET pathway, wherein $\{P_2W_{18}\}$_ne_nH_{CBb} pathways dominate the low reduction states (1–6e^-) and $\{P_2W_{18}\}$_ne_nH_{BCt} preponderate the high reduction states (>6e^-). Consequently, we systematically investigated the hybrid protonation system of $\{P_2W_{18}\}$_ne_nH_{CbBt}, in which both O_b and O_t sites are protonated. The corresponding CPET pathway exhibits a lower $\Delta G^{\neq}$ compared to single-site protonated systems, as the associated electronic reconstruction stabilizes the reduced states configuration and thereby facilitates continued multi-electron storage.[41] Besides, as shown in Figure 2f, the CPET pathways present lower $\Delta G^{\neq}$ than sequential steps of ET under the same reduction degree of $\{P_2W_{18}\}$, suggesting the CPET pathways are kinetically favorable when $\{P_2W_{18}\}$ undergoes proton-coupled electron transfer reactions.[37]

To investigate the redox properties of $\{P_2W_{18}\}$ and its reduced species, the reduction potential was calculated in ET and CPET pathways in Figure 2g. The reduction potentials of $\{P_2W_{18}\}$_1e, $\{P_2W_{18}\}$_2e, $\{P_2W_{18}\}$_3e, and $\{P_2W_{18}\}$_4e are 0.01 V, −0.26 V, −0.47 V, and −0.65 V versus SHE, respectively. However, the obviously negative shift of calculated reduction potentials for $\{P_2W_{18}\}$_ne compared to experimental CV data underscores the critical role of protonation in $\{P_2W_{18}\}$ reduction processes. The reduction potentials for $\{P_2W_{18}\}$_ne_nH_{Cb} species at low reduction states are 0.13 V, 0.12 V, 0.07 V, −0.02 V, and −0.21 V versus SHE, respectively, aligning closely with experimental CV data in Figure 1a. Furthermore, $\{P_2W_{18}\}$_ne_nH_{Bt} species exhibit a significant deviation in calculated reduction potentials,

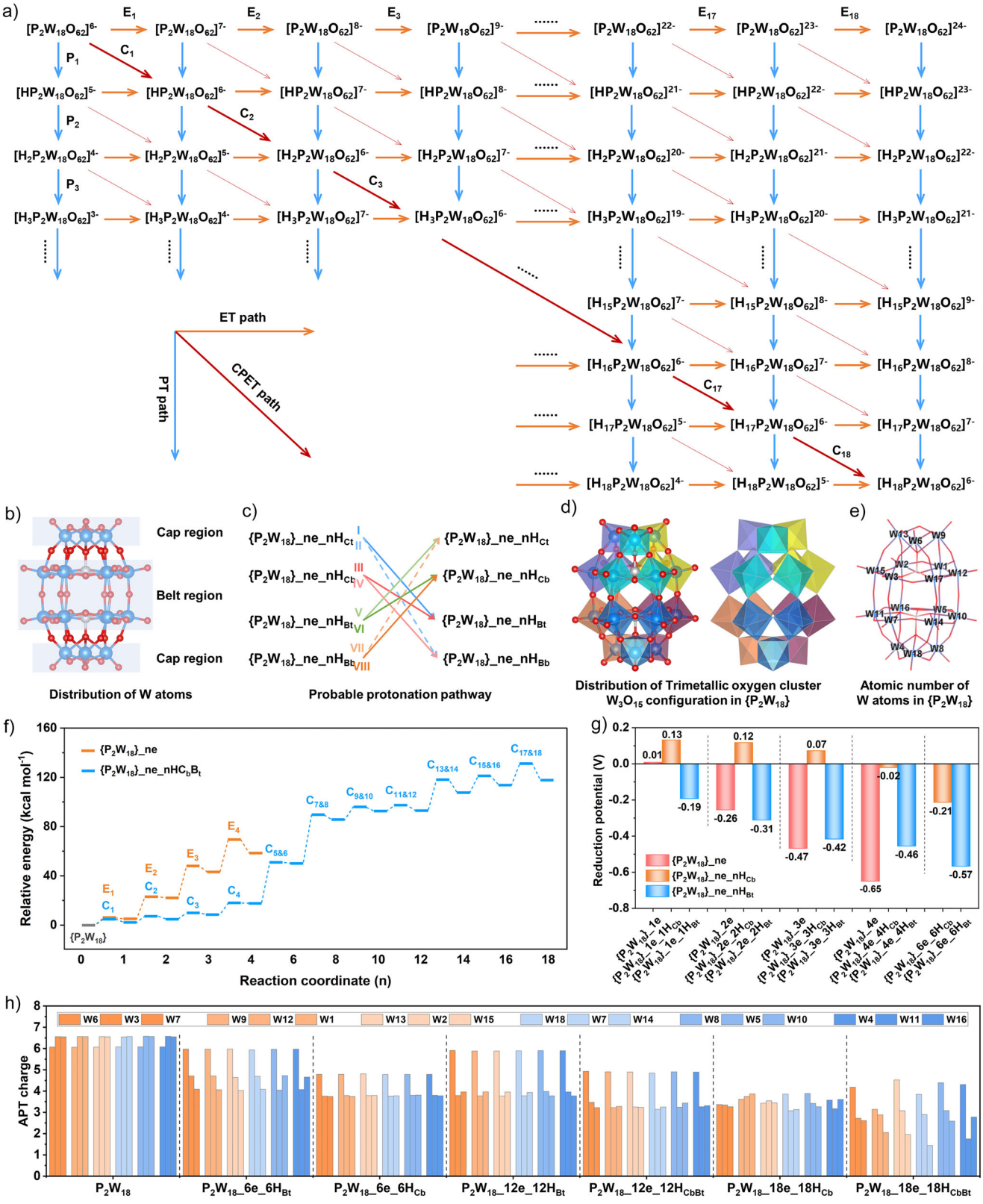

Figure 2. a) Schematic diagram of PCET process for $\{P_2W_{18}\}$. b) Region distribution of W atoms in $\{P_2W_{18}\}$ cluster. c) Probable protonation pathway of $\{P_2W_{18}\}$ reduction processes in PCET pathways. d) Distribution of trimetallic oxygen cluster (W_3O_{15}) configuration in $\{P_2W_{18}\}$. e) Atomic number of W in $\{P_2W_{18}\}$. f) The activation energy network diagram of $\{P_2W_{18}\}$ reduction process in ET pathways, and $\{P_2W_{18}\}$_ne_nH_{CbBt} in CPET pathway. g) The reduction potential of $\{P_2W_{18}\}$_ne_nH_{Cb} and $\{P_2W_{18}\}$_ne_nH_{Bt} at low reduction states ($n = 1$–6). ($\{P_2W_{18}\}$_ne_nH_{Cb}: the bridge oxygen protonation at the "Cap region" of $\{P_2W_{18}\}$ cluster, $\{P_2W_{18}\}$_ne_nH_{Bt}: the terminal oxygen protonation at the "Belt region" of $\{P_2W_{18}\}$ cluster). h) The atomic polar tensor (APT) charge of each W site in the three metal oxygen clusters of $\{P_2W_{18}\}$_ne_nH ($n = 0$, 6, 12, 18).

while $\{P_2W_{18}\}$_ne_nH_{CbBt} species present a more reasonable reduction potential at all reduction states in Table S8. These results confirm that O_b protonation and O_t protonation govern CPET pathways by reducing the reduction potential of the $\{P_2W_{18}\}$_ne_nH reduction species at low reduction states and high reduction states, respectively.

Structurally, as depicted in Figure 2d, $\{P_2W_{18}\}$ cluster features six trimetallic oxygen cluster units (W_3O_{15}) labeled in different colors, with each unit consisting of one "Cap region" W atom and two "Belt region" W atoms connected through the bridging oxygen atoms. The atomic numbering of the 18 W positions in the $\{P_2W_{18}\}$ cluster is presented in Figure 2e. By analyzing the charge of all active sites, it was found that the atomic polar tensor (APT) charge of W and O atoms consistently decreases in CPET pathways. The APT charge of $\{P_2W_{18}\}$, $\{P_2W_{18}\}$_6e_$6H_{Cb}$, $\{P_2W_{18}\}$_12e_$12H_{CbBt}$, and $\{P_2W_{18}\}$_18e_$18H_{CbBt}$ species were compared horizontally, as visually illustrated in Figure 2h. All W atoms in $\{P_2W_{18}\}$ cluster exhibit homogeneous APT charges (+6.4 average), with Cap-W (+6.1) showing lower charge density than Belt-W (+6.6), indicating an intrinsic electronic gradient result from region coordination asymmetry. Nevertheless, the APT charge of W atoms in the "Cap region" exhibits higher than those in the "Belt region" for $\{P_2W_{18}\}$_6e_$6H_{Bt}$, $\{P_2W_{18}\}$_6e_$6H_{Cb}$, $\{P_2W_{18}\}$_12e_$12H_{Bt}$, and $\{P_2W_{18}\}$_12e_$12H_{CbBt}$ clusters, with values of 5.96 versus 4.37, 4.79 versus 3.78, 5.88 versus 3.85, and 4.89 versus 3.28, respectively, demonstrating that electrons preferentially storage in the "Belt region" to achieve the reduction of W atoms in CPET pathways. Furthermore, $\{P_2W_{18}\}$_18e_$18H_{Cb}$ and $\{P_2W_{18}\}$_18e_$18H_{CbBt}$ clusters achieve charge homogenization of W atoms across each trimetallic oxygen cluster unit, confirming the region-selectivity reduction sequence of W atoms in $\{P_2W_{18}\}$ cluster follows "Belt region" to "Cap region".

Overall, electrons preferentially accumulate at the "Belt region" W sites, and protonation tends to switches from bridging O at low reduction states to terminal O at high reduction states, enabling a low-barrier, region-selective CPET pathway that stabilizes the highly reduced $\{P_2W_{18}\}$ cluster.

Structural Evolutions of $\{P_2W_{18}\}$ at Different States-of-Charge (SoC)

To elucidate the structural evolution of $\{P_2W_{18}\}$ electrolyte during deep reduction, FTIR and Raman spectroscopy were used to reveal the structural response of $\{P_2W_{18}\}$_ne electrolytes at different reduced states ($1e^-$, $6e^-$, $12e^-$, $18e^-$), with the original oxidation state ($0e^-$) as the reference. As shown in Figure 3a, the FTIR characteristic peaks located at 1091.9 cm^{-1}, 964.7 cm^{-1}, 912.6 cm^{-1}, and 765.5 cm^{-1} are associated to the P—O_a symmetric stretching vibration, the W=O_t asymmetric stretching vibration, the W—O_b—W asymmetric stretching vibration, and the W—O_c—W bending vibration, respectively, highly consistent with the FTIR results of the $\{P_2W_{18}\}$ powder material (Figures S2a,b). In addition, the newly observed characteristic peaks at 1173.5 cm^{-1} and 1045.7 cm^{-1} are attributed to the antisymmetric stretching vibration signals of the S—O bond in SO_4^{2-} and HSO_4^-,

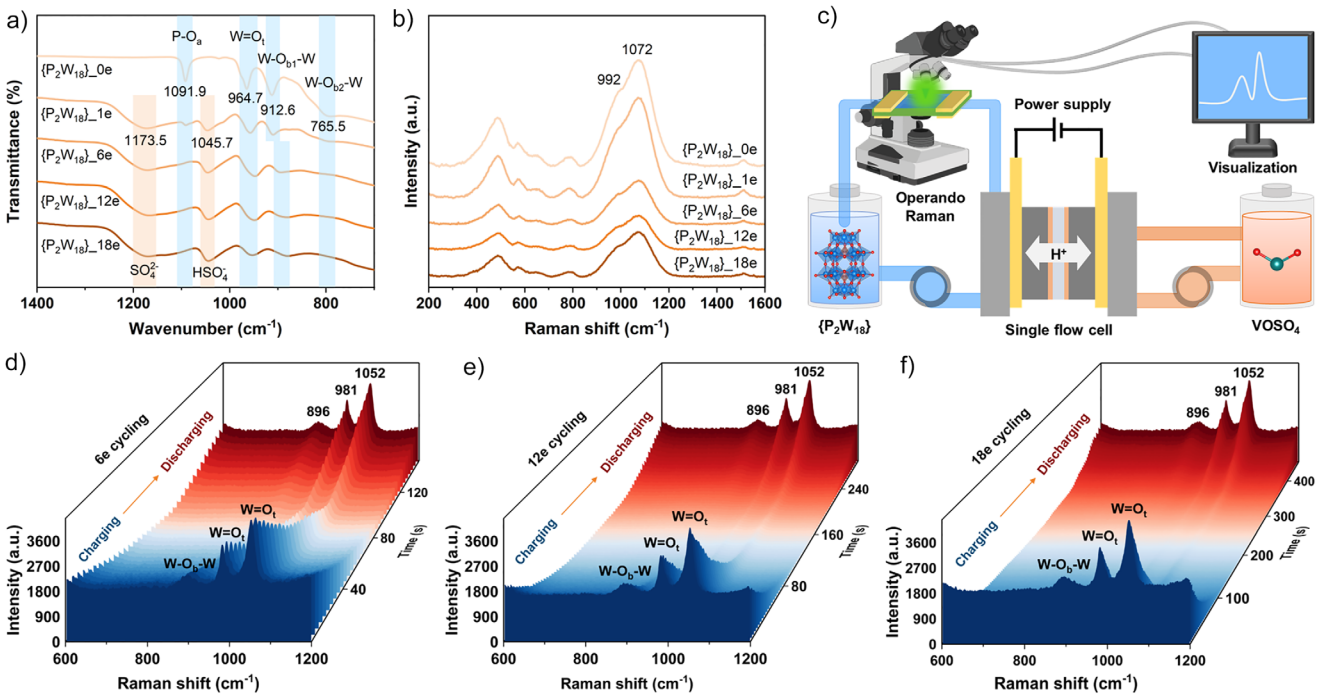

Figure 3. a) FTIR spectrum of the reduced state $\{P_2W_{18}\}$_ne (n = 0, 1, 6, 12, 18). b) Raman spectrum of the reduced state $\{P_2W_{18}\}$_ne (n = 0, 1, 6, 12, 18). c) Schematic diagram of operando Raman for redox flow battery. The 3D plots of operando Raman flow–cell spectrum during the charging-discharging process of the $H_6\{P_2W_{18}\}$-vanadium redox flow batteries (HPVBs) at d) $6e^-$ capacity cycling, e) $12e^-$ capacity cycling, and f) $18e^-$ capacity cycling.

respectively, and fail to be observed in the pristine $\{P_2W_{18}\}$ electrolyte, which is related to the diluted H_2SO_4 medium in $\{P_2W_{18}\}$_ne electrolytes. It is worth noting that the progressive intensity weakening of the FTIR and Raman characteristic peak with increasing SoC is induced by protonation and charge rearrangement of $\{P_2W_{18}\}$ cluster (Figures 3a,b). Notably, the broader Raman peaks of $\{P_2W_{18}\}$_n electrolytes compared to solid samples (Figure S2c,d) originate from the differences in the solvation environment and the molecular motion state in Figure 3b, where the solvation shell effects promote the peak overlap between 1072 cm^{-1} (W═O_t symmetric stretching vibration) and 992 cm^{-1} (W═O_t asymmetric stretching vibration).

Furthermore, operando flow–cell Raman spectroscopy was employed to track the redox chemistry and structural evolution of $\{P_2W_{18}\}$ during the reversible CPET processes under the operation of RFBs, as the schematic diagram depicted in Figure 3c. The charging-discharging processes of $H_6\{P_2W_{18}\}$-vanadium redox flow batteries (HPVBs) correspond to the reduction and reoxidation of $H_6\{P_2W_{18}\}$ negolyte, respectively. As 3D plots shown in Figures 3d-f, the intensity of W═O_t symmetric stretch vibration at 1052 cm^{-1}, W═O_t asymmetric stretch vibration at 981 cm^{-1}, and W─O_b─W stretch vibration at 896 cm^{-1} were gradually decreased until charging the preset capacity ($6e^-$, $12e^-$, and $18e^-$) of $\{P_2W_{18}\}$, and then recovered during the discharging process. It is worth noting that the vibration intensity of W═O_t and W─O_b─W bonds further decreases as the charging depth ($6e^- \rightarrow 12e^- \rightarrow 18e^-$ capacity) increases of $\{P_2W_{18}\}$. Moreover, the evolution of W═O_t and W─O_b bond lengths associated with protonated O sites shows a regular increase with the CPET process of $\{P_2W_{18}\}$ cluster (Tables S9–S14), indicating that the electronic rearrangement and protonation of $\{P_2W_{18}\}$ cluster induce the relaxation of intermediate W─O─H bonds and weaken the stretching vibration intensity of the original bonds. Besides, the characteristic peaks at 1637 cm^{-1} (O─H bending vibration), 3258 cm^{-1} (O─H asymmetric stretching vibration), and 3420 cm^{-1} (O─H symmetric stretching vibration) originate from the dynamic hydrogen-bonding network of hydrated proton (H_3O^+) in the $\{P_2W_{18}\}$ electrolyte (Figure S19). These spectral signatures confirm the CPET process, wherein more stable hydrogen bond interactions are formed between the H_3O^+ and $\{P_2W_{18}\}$ cluster, resulting in a decreased vibration intensity of the hydrogen-bonding network during the charging process of HPVBs. These operando Raman results confirm that $\{P_2W_{18}\}$ cluster exhibits a high structural stability and reversibility during the charging-discharging processes of HPVBs cycling.

Multi-electron Transfer Capacity and Redox Control Steps of $\{P_2W_{18}\}$

To establish standardized analytical criteria, we define the fully reduced state ($18e^-$ transfer) of $\{P_2W_{18}\}$ as 100% state-of-charge (SoC), corresponding to the theoretical electron storage capacity. As illustrated in Figure 4a, SoC percentage and electron transfer count (n) stick to a strict linear proportionality (SoC = 5.56n%), indicating each transferred electron contributes approximately 5.56% SoC (referring to the definitions provided in the reported literature).[16] The overcharge behavior of HPVB was also investigated by setting charging cut-off limits of 24-electron capacity and 1.75 V voltage using 0.2 M $H_6\{P_2W_{18}\}$ negolyte. As shown in Figure S23, the charging process hit the voltage cut-off before reaching the 24-electron capacity, and the subsequent discharging process could only deliver 11.7-electron capacity with 57.9% Coulombic efficiency, consistent with previous reports.[29] It confirms that exceeding the defined 100% SoC of $\{P_2W_{18}\}$ is not feasible under the operational window of RFB system, therefore establishing the capacity cut-off condition is a safety boundary to prevent overcharging. Through stepwise charging-discharging cycling, the HPVBs were assembled with $H_6\{P_2W_{18}\}$ as the negolyte and $VOSO_4$ as posolyte, demonstrating stable multi-electron (1 to 18 e^-) transfer cycling performance during the three-cycle operation at various electron capacities (Figure 4b). The discharge capacity (DC) increased step by step across 54 cycles (over 90.8 h) to 141.87 Ah L^{-1} at 100 mA cm^{-2}, equivalent to 100% SoC of 0.3 M $H_6\{P_2W_{18}\}$ negolyte with 98.5% average coulombic efficiency (CE) and 79.6% energy efficiency (EE). In addition, three distinct plateau regions emerge from the voltage-capacity profile during HPVB charging-discharging cycling processes in Figure 4c. The charging process exhibits three plateaus corresponding to steps of sequential electronic capacity storage of 1–$2e^-$, 3–$4e^-$, and 5–$18e^-$, whereas the three plateaus in the discharging process correspond to steps of sequential electronic capacity release of 1–$2e^-$, 3–$14e^-$, and 15–$18e^-$. These findings conclusively demonstrate the exceptional multi-electron redox capability of $\{P_2W_{18}\}$ cluster, unlocking full $18e^-$ transfer through stepwise cycling, which is a critical advancement beyond conventional POM-based energy storage materials. However, the long-term cycling performance of HPVB at high SoC of $\{P_2W_{18}\}$ still needs to be systematically investigated.

The CPET pathways of $\{P_2W_{18}\}$ reduction involve the participation of multiple electrons and protons, which are specifically composed of 18 single-electron transfer steps connected in series. According to experiments, the dynamic behavior of these consecutive single-electron transfer steps exhibits heterogeneity, resulting in multi-electron transfer reactions may involve one or more control steps (rate-determining steps), which are attributed to electron reconstruction within the $\{P_2W_{18}\}$ cluster or external proton migration.[42] Combined electrochemical tests and the performance correlation of RFBs, we hypothesize that there may be two kinetically controlled steps at the 7th (control step I) and 13th (control step II) electron transfer steps in $\{P_2W_{18}\}$ CPET pathways (Figure S20). CV tests for $\{P_2W_{18}\}$ electrolyte exhibit approximately $6e^-$ transfer (33.3% SoC) under the three-electrode configuration with glassy carbon electrode (active area is 0.07 cm^2) as the working electrode.[30] This limitation for more electron transfer originates from severe concentration polarization (static electrolyte) and limited active sites, resulting in only electron transfer within the control step I could be detected. Nevertheless, under galvanostatic charge-discharge and forced electrolyte convection conditions, the $\{P_2W_{18}\}$ electrolyte could continuously obtain

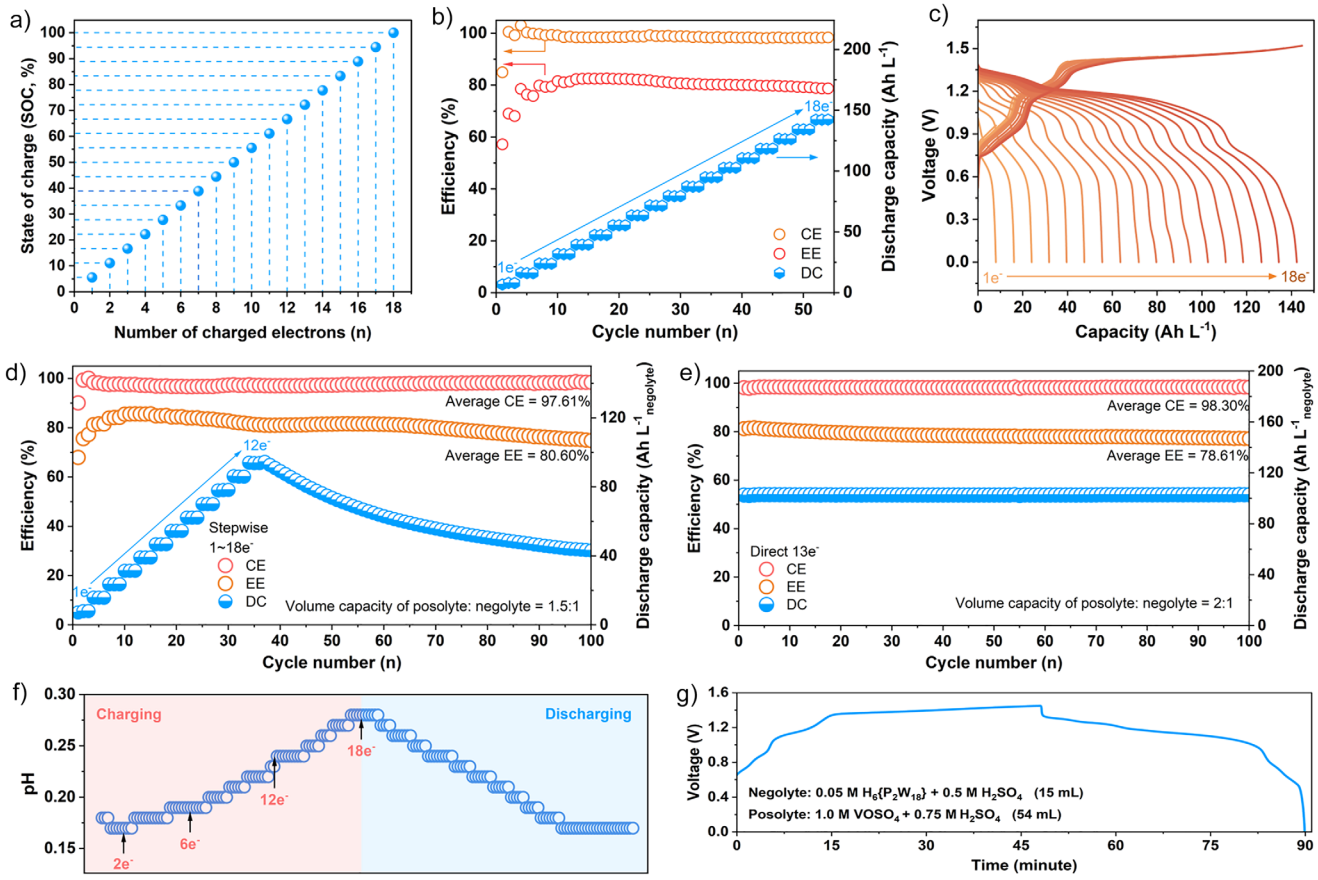

Figure 4. a) Definition of SoC for reduced $\{P_2W_{18}\}$. b) Stepwise charging-discharging performance for $\{P_2W_{18}\}$-based RFB. negolyte: 0.3 M $\{P_2W_{18}\}$ + 1.8 M H_2SO_4; posolyte: 1.5 M $VOSO_4$ + 3.0 M H_2SO_4; the theoretical volumetric capacity of the posolyte is set to be three times of the negolyte. c) The galvanostatic voltage-capacity profiles during the stepwise charging-discharging processes. d) Monitoring of control steps in $\{P_2W_{18}\}$ redox processes under limited proton supply conditions. e) Breakthrough control steps in $\{P_2W_{18}\}$ redox processes under sufficient proton supply conditions. f) Operando pH values during the charging-discharging process of the HPVBs. g) The voltage-time curve during the cycling process of operando pH monitoring.

stable electron supply and electron release at the cathode (carbon felt, active area is 9 cm^2) in the RFB system, making it possible to break through the control step I and achieve more electron transfer (>6e$^-$). Furthermore, it should be noted that $\{P_2W_{18}\}$ clusters undergo reversible redox reactions at the cathode during HPVBs operation. Upon charging, $\{P_2W_{18}\}$ is reduced while protons (H^+) migrate from the anode through the membrane to maintain charge neutrality, thereby completing the current circuit. During discharging, $\{P_2W_{18}\}$ is reoxidized with deprotonation and protons back-diffuse to the anode. This model facilitates the reduction of $\{P_2W_{18}\}$ through CPET pathways during charging, and enables efficient reoxidation-coupled deprotonation of $\{P_2W_{18}\}$ during discharging.

More importantly, the control step II (13e$^-$ step) of $\{P_2W_{18}\}$ reduction will be manifested in the RFB system when the electrolyte capacity matching is insufficient, such as the baseline configuration (negolyte: 0.3 M $H_6\{P_2W_{18}\}$ + 1.8 M H_2SO_4, 8 mL; posolyte: 1.5 M $VOSO_4$ + 3 M H_2SO_4, 43.2 mL; capacity ratio of 1.5:1). Later, the HPVBs was subjected to stepwise electron capacity testing ranging from 1e$^-$ to 18e$^-$, demonstrating stable operation for first 36 cycles (1e$^-$ to 12e$^-$ steps) with maximum DC reaching 93.78 Ah L^{-1}. However, starting from the 13e$^-$ step, a sharp increase in charge voltage polarization triggered progressive DC fading, suggesting that the $\{P_2W_{18}\}$ cluster is in an unstable state with an increased reduction potential due to the "proton starvation". After 100 cycles, the DC ultimately decayed to 43.14 Ah L^{-1} (Figure 4d). Significantly, the charging voltage polarization originally observed at control step II disappeared with adjusted theoretical capacity ratios (capacity of posolyte: negolyte = 3:1) in Figure 4b. Besides, the HPVBs presented remarkable stability by direct charging-discharging at 13e$^-$ capacity during 100 cycles (capacity of posolyte: negolyte = 2:1), where the DC remained at 102.83 Ah L^{-1} without decline (Figure 4e), as well as the average CE and EE were 98.3% and 78.61%, respectively. As shown in Figures 4f,g, the pH evolutions of $H_6\{P_2W_{18}\}$ negolyte during the charging-discharging processes were monitored by an operando pH system (Figure S21), which exhibits distinct pH regimes during HPVB operation. At the initial 2e$^-$ capacity charging process, pH dropped from 0.18 to 0.17 and stabilized, indicating that H^+ accumulated in the solvation shell of $\{P_2W_{18}\}$ and effective protonation may not occurred.[43] For the

$3e^-$ to $18e^-$ charging processes, pH monotonically increases from 0.17 to 0.26, demonstrating proton-coupled reduction where transmembrane H^+ is insufficient, requiring additional proton extraction from the negolyte. The discharge stage as contrast, pH decreases from 0.26 to 0.17, evidencing proton deprotonation from the $\{P_2W_{18}\}$ cluster and re-entering the posolyte through transmembrane transport.

Redox Flow Battery Performance Tests

Guided by the CPET mechanistic insights of $\{P_2W_{18}\}$ cluster, we engineered high-proton-activity $H_6\{P_2W_{18}\}$ negolytes and stepwise charging-discharging protocol for HPVBs to overcome long-standing bottlenecks of "proton starvation" at high SoC of $\{P_2W_{18}\}$ (Table S16). Hence, the cycling performance of HPVB flow cells (Figures S16 and S17) was systematically evaluated at high SoC (66.7% SoC ($12e^-$) and 100% SoC ($18e^-$)) of $\{P_2W_{18}\}$ by direct and stepwise charging-discharging protocols. The HPVB flow cell employs 0.3 M $H_6\{P_2W_{18}\}$ in 1.8 M H_2SO_4 as the negolyte paired with 1.5 M $VOSO_4$ in 3 M H_2SO_4 as the posolyte, ensuring sufficient proton synergy in the CPET pathways of $\{P_2W_{18}\}$ redox process. VO^{2+}/VO_2^+ redox couples exhibit a highly reversible single-electron redox reaction at 0.991 V versus SHE in acidic conditions. At 66.7% SoC of 0.3 M $H_6\{P_2W_{18}\}$ negolyte, HPVB presents excellent rate performance within the current density range of 50 to 300 mA cm^{-2} in Figure 5a,b. The voltage polarization between the charging and discharging platforms exhibited a gradual increase as current density

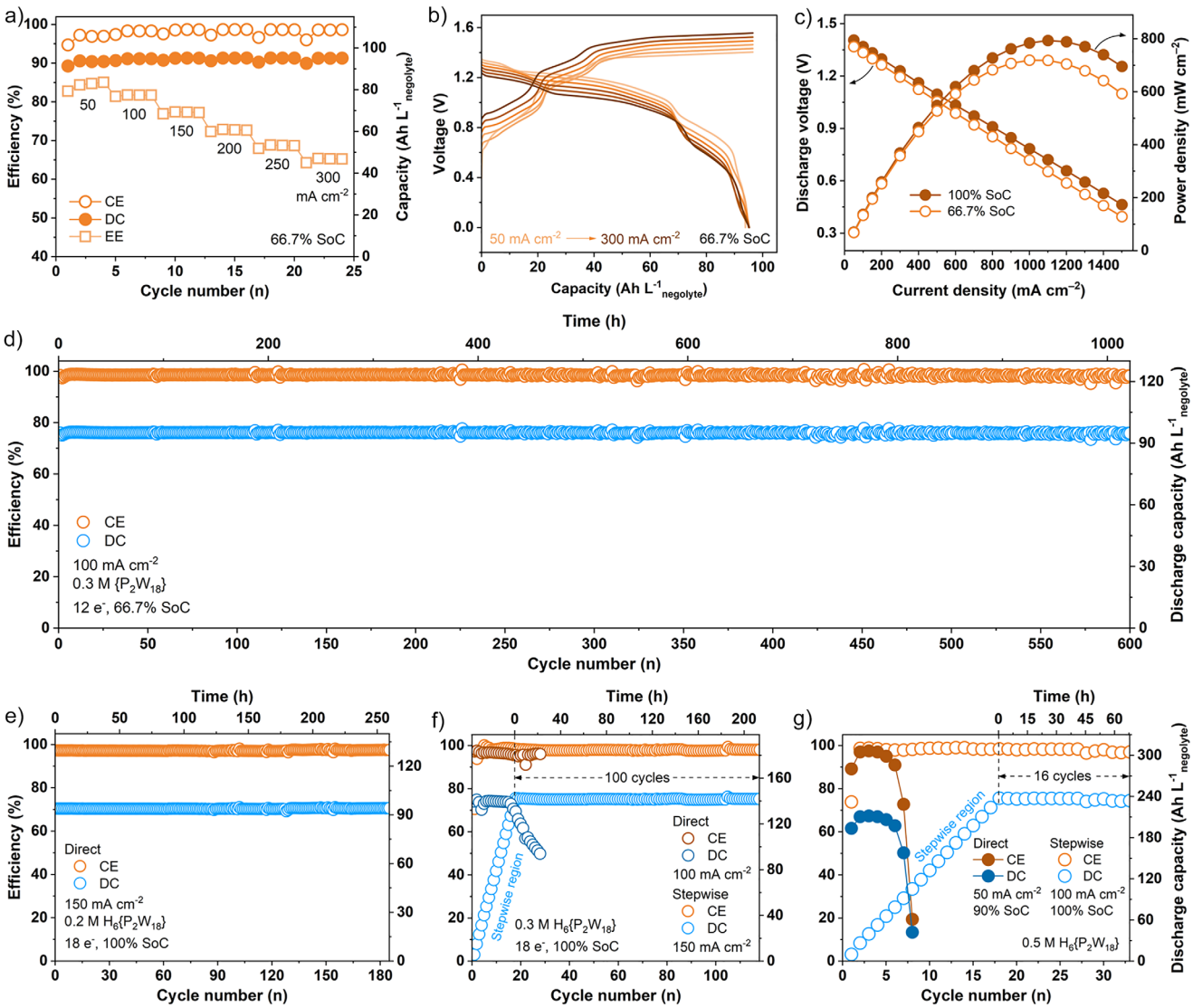

Figure 5. a) Capacity and efficiencies for HPVB flow cells cycling from 50 mA cm^{-2} to 300 mA cm^{-2} at 66.7% SoC of 0.3 M $H_6\{P_2W_{18}\}$ negolyte. b) Galvanostatic voltage-capacity profiles from 50 mA cm^{-2} to 300 mA cm^{-2} at 66.7% SoC of 0.3 M $H_6\{P_2W_{18}\}$ negolyte. c) Discharge polarization curves at 66.7% SoC and 100% SoC of 0.3 M $H_6\{P_2W_{18}\}$ negolyte. d) Discharge capacity (DC) and Coulombic Efficiency (CE) at 100 mA cm^{-2} and 66.7% SoC of 0.3 M $H_6\{P_2W_{18}\}$ negolyte. e) DC and CE of 0.2 M $H_6\{P_2W_{18}\}$ negolyte at 100% SoC by direct charging-discharging protocols. f) DC and CE of 0.3 M $H_6\{P_2W_{18}\}$ negolyte at 100% SoC by direct and stepwise charging-discharging protocols. g) DC and CE of 0.5 M $H_6\{P_2W_{18}\}$ negolyte at 100% SoC by direct and stepwise charging-discharging protocol.

escalated, causing a systematic decline in EE from 85.05% to 65.37%. In addition, a high-power density of 719.2 mW cm^{-2} and 793.22 mW cm^{-2} was achieved at 66.7% SoC and 100% SoC of 0.3 M $H_6\{P_2W_{18}\}$ negolyte, respectively (Figure 5c). Furthermore, as shown in Figure 5d, the HPVB flow cell in the direct charging-discharging protocol demonstrated exceptional cycling stability with no capacity decay after 600 cycles (over 1020 h) at 100 mA cm^{-2} and 66.7% SoC of 0.3 M $H_6\{P_2W_{18}\}$ negolyte, delivering average DC of 95.04 Ah L^{-1} and CE of 98.50%.

Significantly, the HPVB flow cell in the direct charging-discharging protocol exhibited an average DC of 93.84 Ah L^{-1} and CE of 97.27% at 100% SoC of 0.2 M $H_6\{P_2W_{18}\}$ negolyte over 180 cycles (over 250 h) (Figure 5e). However, the HPVB flow cell experienced rapid capacity decay at 100% SoC of 0.3 M $H_6\{P_2W_{18}\}$ negolyte when operating in direct charging-discharging protocol in Figure 5f. This result is attributed to insufficient proton supply versus high demand in the charging process, which subsequently triggered the cut-off voltage. The excessive accumulation of electrons may cause distortion of the WO_6 octahedron, resulting in the deactivation of partial $\{P_2W_{18}\}$ clusters and battery failure in the form of capacity decay during the continued cycling process. Furthermore, we designed a stepwise charging-discharging protocol for the HPVB flow cell to ensure stable operation of $H_6\{P_2W_{18}\}$ negolyte at 100% SoC, overcoming the initial proton starvation conditions caused by limited solubility of higher concentration $H_6\{P_2W_{18}\}$ in acidic media (Figure 5f,g). Encouragingly, the 0.3 M $H_6\{P_2W_{18}\}$ negolyte demonstrated excellent DC of 141.75 Ah L^{-1} and energy density (ED) of 137.13 Wh L^{-1} at 150 mA cm^{-2} with CE of 97.95% (Figure 5f). Most importantly, as depicted in Figure 5f, the 0.5 M $H_6\{P_2W_{18}\}$ negolyte demonstrated a record-breaking DC of 236.03 Ah L^{-1} and ED of 239.02 Wh L^{-1} at 100 mA cm^{-2} and 100%SoC with CE of 97.86% (Table S17). The operando pH results indicate that there may be slight incomplete deprotonation of $H_6\{P_2W_{18}\}$ during the discharge stage, which in turn promotes $H_6\{P_2W_{18}\}$ negolyte cycling at 100% SoC through cumulative effects. Therefore, the stepwise charging-discharging protocol helps to reduce the high proton barrier of $\{P_2W_{18}\}$ at high SoC, breaking through the bottleneck of "proton starvation" and effectively improving the cycling stability of $\{P_2W_{18}\}$-based RFBs. As summarized in Tables S18 and S19, $H_6\{P_2W_{18}\}$ negolytes developed in this work delivers exceptional performance metrics. Most notably, its discharge capacity and energy density significantly exceeds POM-RFBs (typically DC $<$ 80 Ah L^{-1}) and many state-of-the-art RFB systems, such as all–vanadium (ED $<$ 40 Wh L^{-1}),[44] Zn–Br (ED $\leq$ 152 Wh L^{-1}),[17] advanced organic (ED $<$ 60 Wh L^{-1}),[23] and redox-targeting (liquid-solid, ED $\leq$ 97.4 Wh L^{-1})[45] RFBs, warranting $H_6\{P_2W_{18}\}$ as an ideal POM candidate for high-energy-density RFB application. FTIR and Raman results, as well as the High-Resolution Mass Spectrometry (HRMS) results, confirmed that the structure of the $\{P_2W_{18}\}$ cluster remained stable before and after the cycling process (Figures S24 and S25). Furthermore, the high-proton-activity $H_6\{P_2W_{18}\}$ negolytes exhibit high conductivity (>436 mS cm^{-1}) at various concentrations (Table S20), supporting the CPET process during $\{P_2W_{18}\}$ reduction. It is also worth mentioning that protons are effectively consumed at the active site based on the CPET mechanism of $\{P_2W_{18}\}$, thereby to some extent suppressing the local proton availability for hydrogen evolution reaction during the HPVB cycling. While the viscosity increases with the SoC, the highest viscosity of 0.5 M $H_6\{P_2W_{18}\}$ negolyte at 100% SoC (82.52 mPa·s at 25 °C, Table S20) is similar to the reported 0.5 M $H_6\{P_2W_{18}\}$ negolyte at 33.3%SoC (75.01 mPa·s at −20 °C)[30] and 1.5 M AQ-1,8–3E-OH negolyte (~90 mPa·s at 37 °C).[46] To advance toward practical applications, future work needs to focus on mitigating the insufficient proton supply at high concentrations and the rising viscosity at high SoC of $H_6\{P_2W_{18}\}$ negolyte through dedicated electrolyte engineering.

Conclusion

This study resolves the long-standing challenge of achieving high-SoC operation in POM electrolytes through an integrated approach, which combines CPET mechanistic elucidation, high-proton-activity electrolyte engineering, and stable cycling redox flow battery validation. Specifically, we demonstrate that protonation at terminal and bridging O sites stabilizes reduced W sites of $[P_2W_{18}O_{62}]^{6-}$ ($\{P_2W_{18}\}$) cluster via region-selective CPET processes by synergistic Marcus theory, first-principles density functional theory (DFT) calculations and ab initio molecular dynamics (AIMD) simulations. Operando Raman spectroscopy and operando pH monitoring further confirm this proton-coupled reversibility across $\{P_2W_{18}\}$ redox processes. Guided by these mechanistic insights, we designed high-proton-activity $H_6\{P_2W_{18}\}$ negolytes and implemented the stepwise charging-discharging protocol to overcome the bottlenecks of proton starvation and poor stability at high SoC of $\{P_2W_{18}\}$. The resulting RFBs demonstrate superior cycling performance at high SoC of $H_6\{P_2W_{18}\}$ negolyte, without discharge capacity decay (95.04 Ah L^{-1}) after 600 cycles (over 1020 h) by direct charging-discharging protocol at 66.7% SoC of 0.3 M $H_6\{P_2W_{18}\}$ negolyte, and excellent discharge capacity of 141.75 Ah L^{-1} at 100% SoC of 0.3 M $H_6\{P_2W_{18}\}$ negolyte by stepwise charging-discharging protocol, as well as a record-breaking discharge capacity of 236.03 Ah L^{-1} and energy density of 239.02 Wh L^{-1} at 100% SoC of 0.5 M $H_6\{P_2W_{18}\}$ negolyte. These findings position $\{P_2W_{18}\}$ as a highly promising multi-electron redox active species for high-energy-density RFB, offering an applicable paradigm to unlock the full SoC of POM-RFBs via concerted proton-electron transfer.

Supporting Information

The authors have cited additional references within the Supporting Information.[47–57]

Acknowledgements

This work was financially supported by the Joint Funds of the National Natural Science Foundation of China

(No. U22A20170), National Key Research and Development Program of China (No. 2022YFC3900900), Major Research Program integration project of National Natural Science Foundation of China (No. 92462307), Innovation-Driven Project of Central South University (No. 2023CXQD002), the Changsha Science and Technology Project (Changsha Outstanding Innovative Youth Training Program), the Fundamental Research Funds for the Postgraduate Innovative Project of Central South University Project (No. 2024ZZTS0430), the Wuhan Zhisheng New Energy Co., Ltd. for the customized design of single redox flow cells, and the High-Performance Computing Centers of Central South University.

Conflict of Interests

The authors declare no conflict of interest.

Data Availability Statement

The data that support the findings of this study are available from the corresponding author upon reasonable request.

Keywords: Concerted proton-electron transfer · High-energy-density · Polyoxometalates · Redox flow battery · State-of-charge

[1] S. Chen, *Nature* **2025**, https://doi.org/10.1038/d41586-025-01113-z.
[2] International Renewable Energy Agency (IRENA). Global Renewables Outlook: Energy transformation 2050, https://www.irena.org/publications/2020/Apr/Global-Renewables-Outlook-2020, **2020**.
[3] International Energy Agency (IEA). Renewables 2024, Analysis and forecast to 2030, **2024**, https://www.iea.org/reports/renewables-2024.
[4] W. Wang, B. Yuan, Q. Sun, R. Wennersten, *J. Energy Storage.* **2022**, *52*, 104812.
[5] Z. Zhao, X. Liu, M. Zhang, L. Zhang, C. Zhang, X. Li, G. Yu, *Chem. Soc. Rev.* **2023**, *52*, 6031–6074, https://doi.org/10.1039/D2CS00765G.
[6] Y. Yao, J. Lei, Y. Shi, F. Ai, Y.-C. Lu, *Nat. Energy.* **2021**, *6*, 582–588.
[7] E. Sanchez-Diez, E. Ventosa, M. Guarnieri, A. Trovo, C. Flox, R. Marcilla, F. Soavi, P. Mazur, E. Aranzabe, R. Ferret, *J. Power Sources.* **2021**, *481*, 228804, https://doi.org/10.1016/j.jpowsour.2020.228804.
[8] R. Huang, S. Liu, Z. He, W. Zhu, G. Ye, Y. Su, W. Deng, J. Wang, *Adv. Funct. Mater.* **2022**, *32*, 2111661.
[9] L. Zhi, C. Liao, P. Xu, G. Li, Z. Yuan, X. Li, *Angew. Chem. Int. Ed.* **2024**, *63*, e202412559.
[10] S. Belongia, X. Wang, X. Zhang, *Adv. Funct. Mater.* **2024**, *34*, 2302077, https://doi.org/10.1002/adfm.202302077.
[11] J. Lei, Y. Yao, Z. Wang, Y.-C. Lu, *Energy Environ. Sci.* **2021**, *14*, 4418–4426.
[12] B. Fang, S. Iwasa, Y. Wei, T. Arai, M. Kumagai, *Electrochim. Acta.* **2002**, *47*, 3971–3976, https://doi.org/10.1016/S0013-4686(02)00370-5.
[13] Y. K. Zeng, T. S. Zhao, X. L. Zhou, L. Wei, H. R. Jiang, *J. Power Sources.* **2016**, *330*, 55–60, https://doi.org/10.1016/j.jpowsour.2016.08.107.
[14] E. Shittu, R. Suman, M. K. Ravikumar, A. K. Shukla, G. Zhao, S. Patil, J. Baker, *J. Cleaner Prod.* **2022**, *337*, 130503, https://doi.org/10.1016/j.jclepro.2022.130503.
[15] C. Xie, Y. Liu, W. Lu, H. Zhang, X. Li, *Energy Environ. Sci.* **2019**, *12*, 1834–1839.
[16] G. Choi, P. Sullivan, X.-L. Lv, W. Li, K. Lee, H. Kong, S. Gessler, J. R. Schmidt, D. Feng, *Nature* **2024**, *635*, 89–95, https://doi.org/10.1038/s41586-024-08079-4.
[17] Y. Xu, T. Li, Z. Peng, C. Xie, X. Li, *Nat. Energy.* **2025**, *10*, 1470–1481.
[18] J. Lei, Y. Zhang, Y. Yao, Y. Shi, K. L. Leung, J. Fan, Y.-C. Lu, *Nat. Energy.* **2023**, *8*, 1355–1364.
[19] Z. Li, Y.-C. Lu, *Nat. Energy.* **2021**, *6*, 517–528.
[20] M. Ding, H. Fu, X. Lou, M. He, B. Chen, Z. Han, S. Chu, B. Lu, G. Zhou, C. Jia, *ACS Nano* **2023**, *17*, 16252–16263, https://doi.org/10.1021/acsnano.3c06273.
[21] D. G. Kwabi, K. Lin, Y. Ji, E. F. Kerr, M.-A. Goulet, D. De Porcellinis, D. P. Tabor, D. A. Pollack, A. Aspuru-Guzik, R. G. Gordon, M. J. Aziz, *Joule* **2018**, *2*, 1894–1906, https://doi.org/10.1016/j.joule.2018.07.005.
[22] H. Li, H. Fan, B. Hu, L. Hu, G. Chang, J. Song, *Angew. Chem. Int. Ed.* **2021**, *60*, 26971–26977, https://doi.org/10.1002/anie.202110010.
[23] G. X. Ge, C. K. Mu, Y. G. Wang, C. K. Zhang, X. F. Li, *J. Am. Chem. Soc.* **2025**, *147*, 4790–4799.
[24] M. Han, W. Sun, W. Hu, Y. Liu, J. Chen, C. Zhang, J. Li, *Energy Storage Mater.* **2024**, *71*, 103576, https://doi.org/10.1016/j.ensm.2024.103576.
[25] M. Pascual-Borràs, E. Arca, H. Yoshikawa, T. Penfold, P. G. Waddell, R. J. Errington, *J. Am. Chem. Soc.* **2024**, *146*, 26485–26496, https://doi.org/10.1021/jacs.4c09998.
[26] T. Zhao, N. L. Bell, G. Chisholm, B. Kandasamy, D.-L. Long, L. Cronin, *Energy Environ. Sci.* **2023**, *16*, 2603–2610, https://doi.org/10.1039/D3EE00569K.
[27] H. D. Pratt, III, N. S. Hudak, X. Fang, T. M. Anderson, *J. Power Sources.* **2013**, *236*, 259–264, https://doi.org/10.1016/j.jpowsour.2013.02.056.
[28] Y. Liu, S. Lu, H. Wang, C. Yang, X. Su, Y. Xiang, *Adv. Energy Mater.* **2017**, *7*, 1601224.
[29] J.-J. Chen, M. D. Symes, L. Cronin, *Nat. Chem.* **2018**, *10*, 1042–1047.
[30] F. Ai, Z. Wang, N.-C. Lai, Q. Zou, Z. Liang, Y.-C. Lu, *Nat. Energy.* **2022**, *7*, 417–426.
[31] T. Feng, H. Wang, Y. Liu, J. Zhang, Y. Xiang, S. Lu, *J. Power Sources.* **2019**, *436*, 226831, https://doi.org/10.1016/j.jpowsour.2019.226831.
[32] W. Li, W. Xu, Z. Sun, L. Tang, G. Xu, X. He, Y. Deng, W. Sun, B. Zhou, J. Song, W. Liu, *Nat. Commun.* **2025**, *16*, 4654.
[33] J. Friedl, M. V. Holland-Cunz, F. Cording, F. L. Pfanschilling, C. Wills, W. McFarlane, B. Schricker, R. Fleck, H. Wolfschmidt, U. Stimming, *Energy Environ. Sci.* **2018**, *11*, 3010–3018, https://doi.org/10.1039/C8EE00422F.
[34] L. Yang, Y. Hao, J. Lin, K. Li, S. Luo, J. Lei, Y. Han, R. Yuan, G. Liu, B. Ren, J. Chen, *Adv. Mater.* **2022**, *34*, 2107425, https://doi.org/10.1002/adma.202107425.
[35] R. Tyburski, T. Liu, S. D. Glover, L. Hammarstrom, *J. Am. Chem. Soc.* **2021**, *143*, 560–576, https://doi.org/10.1021/jacs.0c09106.
[36] C. Costentin, D. H. Evans, M. Robert, J.-M. Savéant, P. S. Singh, *J. Am. Chem. Soc.* **2005**, *127*, 12490–12491, https://doi.org/10.1021/ja053911n.
[37] D. Langford, R. Rohr, S. Bauroth, A. Zahl, A. Franke, I. Ivanović-Burmazović, D. M. Guldi, *Nat. Chem.* **2025**, *17*, 847–855.

[38] M. Sadakane, E. Steckhan, *Chem. Rev.* **1998**, *98*, 219–238, https://doi.org/10.1021/cr960403a.
[39] E. Sum, M. Skyllas-Kazacos, *J. Power Sources.* **1985**, *15*, 179–190, https://doi.org/10.1016/0378-7753(85)80071-9.
[40] T. Lu, F. Chen, *J. Comput. Chem.* **2012**, *33*, 580–592, https://doi.org/10.1002/jcc.22885.
[41] J.-J. Chen, L. Vila-Nadal, A. Sole-Daura, G. Chisholm, T. Minato, C. Busche, T. Zhao, B. Kandasamy, A. Y. Ganin, R. M. Smith, I. Colliard, J. J. Carbo, J. M. Poblet, M. Nyman, L. Cronin, *J. Am. Chem. Soc.* **2022**, *144*, 8951–8960, https://doi.org/10.1021/jacs.1c10584.
[42] D. L. S. LI, *Electrochemical Principle* (Ed: Y. Feng), Beihang University Press, Beijing, **2021**, Vol. *4*, pp. 191–196.
[43] L.-P. Cui, S. Zhang, Y. Zhao, X.-Y. Ge, L. Yang, K. Li, L.-B. Feng, R.-G. Li, J.-J. Chen, *Nat. Commun.* **2025**, *16*, 3674, https://doi.org/10.1038/s41467-025-58622-8.
[44] R. Huang, S. Liu, Z. He, G. Ye, W. Zhu, H. Xu, J. Wang, *ACS Nano* **2023**, *17*, 19098–19108, https://doi.org/10.1021/acsnano.3c05037.
[45] Y. Chen, M. Zhou, Y. Xia, X. Wang, Y. Liu, Y. Yao, H. Zhang, Y. Li, S. Lu, W. Qin, X. Wu, Q. Wang, *Joule* **2019**, *3*, 2255–2267, https://doi.org/10.1016/j.joule.2019.06.007.
[46] S. Jin, Y. Jing, D. G. Kwabi, Y. Ji, L. Tong, D. De Porcellinis, M.-A. Goulet, D. A. Pollack, R. G. Gordon, M. J. Aziz, *ACS Energy Lett.* **2019**, *4*, 1342–1348, https://doi.org/10.1021/acsenergylett.9b00739.
[47] I.-M. Mbomekalle, Y. W. Lu, B. Keita, L. Nadjo, *Inorg. Chem. Commun.* **2004**, *7*, 86–90, https://doi.org/10.1016/j.inoche.2003.10.011.
[48] M. J. Frisch, G. W. Trucks, H. B. Schlegel, G. E. Scuseria, M. A. Robb, J. R. Cheeseman, G. Scalmani, V. Barone, G. A. Petersson, H. Nakatsuji, X. Li, M. Caricato, A. V. Marenich, J. Bloino, B. G. Janesko, R. Gomperts, B. Mennucci, H. P. Hratchian, J. V. Ortiz, A. F. Izmaylov, J. L. Sonnenberg, D. Williams-Young, F. Ding, F. Lipparini, F. Egidi, J. Goings, B. Peng, A. Petrone, T. Henderson, D. Ranasinghe, et al., *Gaussian 16, Revision A.03*, Gaussian, Inc., Wallingford CT, **2016**.
[49] W. Humphrey, A. Dalke, K. Schulten, *J. Mol. Graphics.* **1996**, *14*, 33–38, https://doi.org/10.1016/0263-7855(96)00018-5.
[50] K. Momma, F. Izumi, *J. Appl. Crystallogr.* **2011**, *44*, 1272–1276, https://doi.org/10.1107/S0021889811038970.
[51] M. Isegawa, F. Neese, D. A. Pantazis, *J. Chem. Theory Comput.* **2016**, *12*, 2272–2284, https://doi.org/10.1021/acs.jctc.6b00252.
[52] G. Kresse, J. Furthmüller, *Comput. Mater. Sci.* **1996**, *6*, 15–50, https://doi.org/10.1016/0927-0256(96)00008-0.
[53] L. Yang, S. Zhang, K. Li, H. Wu, T. Wu, D. Wu, J. Chen, *Energy Storage Mater.* **2024**, *65*, 103149.
[54] Y. Liu, G.-H. Wen, J. Liang, S.-S. Bao, J. Wei, H. Wang, P. Zhang, M. Zhu, Q. Jia, J. Ma, L.-M. Zheng, Z. Jin, *ACS Energy Lett.* **2023**, *8*, 387–397, https://doi.org/10.1021/acsenergylett.2c02121.
[55] Z.-F. Chen, Y.-L. Yang, C. Zhang, S.-Q. Liu, J. Yan, *J. Energy Storage.* **2021**, *35*, 102281, https://doi.org/10.1016/j.est.2021.102281.
[56] F. Xing, Q. Fu, F. Xing, J. Zhao, H. Y. Long, T. Liu, X. F. Li, *J. Am. Chem. Soc.* **2024**, *146*, 26024–26033, https://doi.org/10.1021/jacs.4c04951.
[57] M. Q. Gao, M. Salla, Y. X. Song, Q. Wang, *Angew. Chem. Int. Ed.* **2022**, *61*, e202208223.

Manuscript received: August 28, 2025
Revised manuscript received: January 05, 2026
Manuscript accepted: January 06, 2026
Version of record online: ■■, ■■